Chalcogenide Letters Vol. 22, No. 12, December 2025, p. 987-997

Theoretical Simulation of the Physical Properties of Solar Energy Material α-Cu_2Se

S. H. Fan[1,*], Y. S. Song[1], H. J. Hou[1], H. L. Guo[2] and S. R. Zhang[3]

[1]School of Materials Science and Engineering, Yancheng Institute of Technology, Yancheng, 224051, China
[2]College of Electronic and Information Engineering, Yangtze Normal University, Fuling, Chongqing, 408000, China
[3]Department of Optoelectronics, Huaihua University, Huaihua, 418000, China
*Corresponding Author: S. H. Fan. Email: dahaitg@163.com

Received: 10 September 2025; Accepted: 1 December 2025

ABSRACT: Using first-principles calculations, the physical behavior of α-Cu_2Se are thoroughly examined. The computed structural parameters align closely with experimental data. Through computational analysis, the electronic properties for α-Cu_2Se are determined. Additionally, mechanical characteristics-including bulk modulus *B*, shear modulus *G*, Young's modulus E, and *B*/*G* are evaluated under varying pressure conditions. Furthermore, the optical properties are investigated. The study reveals that α-Cu_2Se exhibits a direct bandgap of 0.782 eV, indicating its promising potential for optoelectronic applications.

KEYWORDS: α-Cu_2Se; electronic structure; optical properties; elastic

1 Introduction

Within the evolving field of materials science, copper selenide (α-Cu_2Se) has garnered considerable scholarly attention due to its exceptional physical characteristics and diverse technological applications [1–3]. As a binary chalcogenide, α-Cu_2Se is capable of forming multiple polymorphic structures, each characterized by a unique atomic arrangement that influences its distinct electrical, optical, and thermal behaviors. Theoretical approaches have been instrumental in uncovering the fundamental principles that govern the performance of this material. Some theoretical methods have been widely utilized to explore its band structure, highlighting a variable bandgap that enhances its effectiveness in thermoelectric and solar energy conversion systems [4,5]. For example, Mikael et al. [6] employed DFT simulations to examine bandgap variations among different α-Cu_2Se polymorphs, offering key insights into its thermoelectric behavior. Additionally, computational studies have contributed to the understanding of phase transformations in α-Cu_2Se. Zhang et al. conducted high-pressure in XRD, supported by theoretical calculations, identifying four distinct phases of Cu_2Se under pressures up to 42.1 GPa [7]. These computational models assist in determining the conditions that trigger phase transitions, thereby supporting the development of more effective α-Cu_2Se-based technologies. Nevertheless, certain aspects of α-Cu_2Se's structural and electronic behavior remain insufficiently explored. The intricate relationship between its crystal lattice, electronic features, and optical responses necessitates further theoretical investigation. This work seeks to address these unresolved issues through comprehensive computational analysis, with the goal of enhancing fundamental insights and facilitating the development of advanced α-Cu_2Se-based materials and devices for future technological applications.

https://doi.org/10.15251/CL.2025.2212.987

2 Simulation Methods

Throughout all the investigations carried out in this study, the projector augmented-wave (PAW) pseudopotentials [8] were consistently applied, along with the Perdew-Burke-Ernzerhof (PBE) formulation [9] under the generalized gradient approximation (GGA), as implemented in the VASP code [10]. Electronic properties were carried out utilizing the CASTEP code [11,12]. The structural model employed the Vanderbilt ultrasoft pseudopotential approach [13], with a energy cutoff of 400.0 eV applied. For the cubic α-Cu_2Se structure, a 5 × 5 × 5 *k*-point grid was generated using the Monkhorst-Pack sampling method.

3 Results and Discussion

3.1 Structural Optimization

In this study, the cubic phase of α-Cu_2Se was selected. Table 1 presents a comparison between the calculated lattice constants *a* of α-Cu_2Se in this work and previously reported experimental values [6,14]. Since the PBE-GGA method yields results closest to experimental data with the smallest deviation, it demonstrates higher accuracy and reliability. Therefore, this method is employed in all subsequent computational procedures. In Fig. 1, the lattice parameter *a* of α-Cu_2Se steadily diminishes as pressure increases, reflecting a proportional decrease in the overall unit cell volume. This trend can be attributed to the enhanced interatomic interactions under elevated external pressure, leading to lattice compression and a reduction in bond lengths.

Table 1: The obtained a (Å), dense ρ (g/cm^3) and Volume (Å^3) α-Cu_2Se varying pressure conditions.

Pressure (GPa)		*a* (Å)	*ρ* (g/cm^3)	*V* (Å^3)
0	This work	5.7598	7.1625	191.083
	Theo. [6]	5.661		
	Theo. [6]	5.844		
	Exp. [14]	5.759		
10	This work	5.6584	7.5545	181.168
20	This work	5.5338	8.0764	169.461
30	This work	5.4390	8.5061	160.900
40	This work	5.3618	8.8788	154.146
50	This work	5.2970	9.2087	148.624

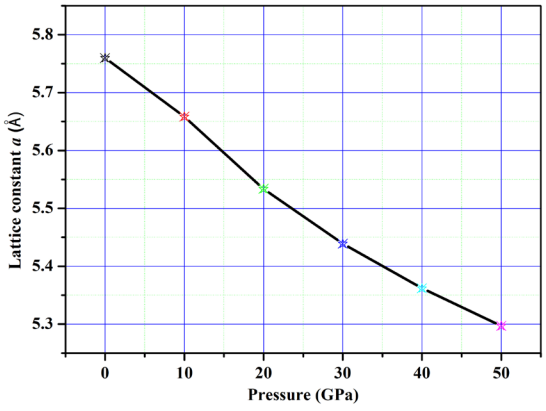

Figure 1: Optimized lattice parameter a of α-Cu_2Se under varying pressure conditions.

3.2 Electronic Structure

The corresponding band structure was calculated using the GGA-PBE approach, as displayed in Fig. 2a. The computed band gap is 0.372 eV, which significantly deviates from the reported value of 1.2 eV [6].

This discrepancy is commonly attributed to the inherent limitation of DFT-based GGA methods, particularly for semiconductors or insulators with strong electron correlations, such as α-Cu_2Se. These methods tend to underestimate the band gap because they fail to adequately account for excited-state effects. Nevertheless, the DFT-GGA approach remains effective in describing the overall electronic structure of α-Cu_2Se. Consequently, the band structure illustrated in Fig. 2a.

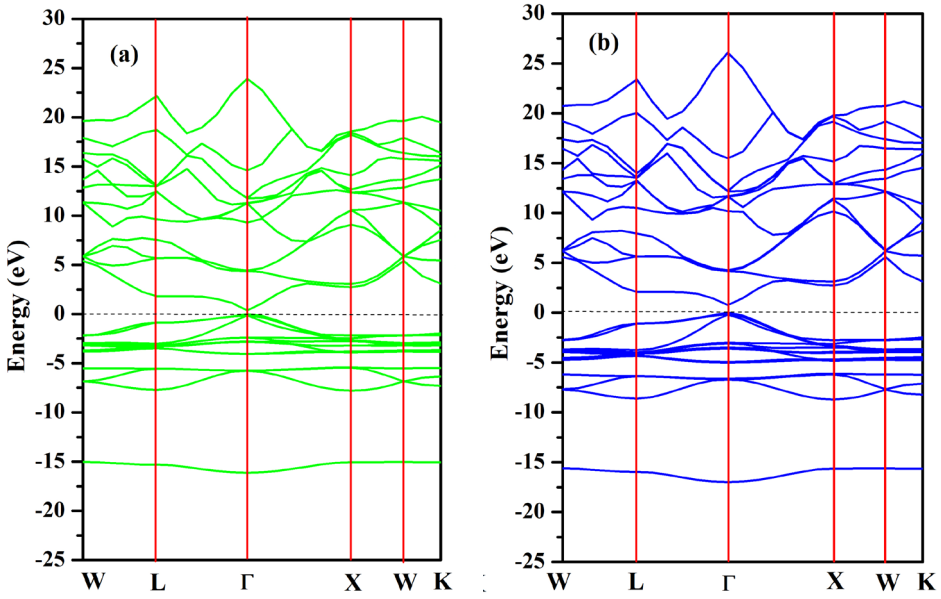

Figure 2: The band structure of α-Cu_2Se. (a) Unmodified band strucure; (b) The modified band structure

To align the theoretical band gap with the reported value of 0.782 eV, a scissors operator (x = 1.171) was employed to adjust the calculated band gap. As illustrated in Fig. 2b, after the correction, confirming that α-Cu_2Se possesses a direct band gap of 1.2 eV.

Fig. 3a displays both the $\varepsilon_1(\omega)$ and $\varepsilon_2(\omega)$. The dominant peak in the imaginary part $\varepsilon_2(\omega)$ appears at approximately 5.1 eV. Key features in the real part of the spectrum include a peak of magnitude 10.53 at around 3.09 eV, followed by a rapid decrease within the energy range of 2.43 eV to 7.82 eV, where the values become negative. A minimum is observed near 9.91 eV, after which the real part gradually rises toward zero. A critical parameter in this analysis is the zero-frequency limit. As a result, the $\varepsilon_1(0)$ is approximately 29.95. Fig. 3b presents the *n* and *k* of α-Cu_2Se. Materials exhibiting a high refractive index typically demonstrate significant optical nonlinearity. The zero-frequency refractive index, *n*(0), is determined to be 5.49. Within the transparent region, it increases with photon energy, reaching a peak of 2.85 near 2.5 eV, after which it declines to a minimum at 14.9 eV. The extinction coefficient reaches its maximum at 6.05 eV, indicating that optical absorption is particularly strong at this energy level. This aligns with the direct correlation between the extinction coefficient and the absorption coefficient, which is mathematically represented by the equation:

$$\alpha = \frac{4\pi k}{\lambda} \tag{1}$$

As shown in Fig. 4a, in the low-energy region, the absorption coefficient *a* increases rapidly, a behavior typical of semiconductors and insulators. Additionally, the computed optical reflectivity is illustrated in Fig. 4b. The reflectivity reaches a peak of about 52% at an energy level of 9.89 eV for α-Cu_2Se.

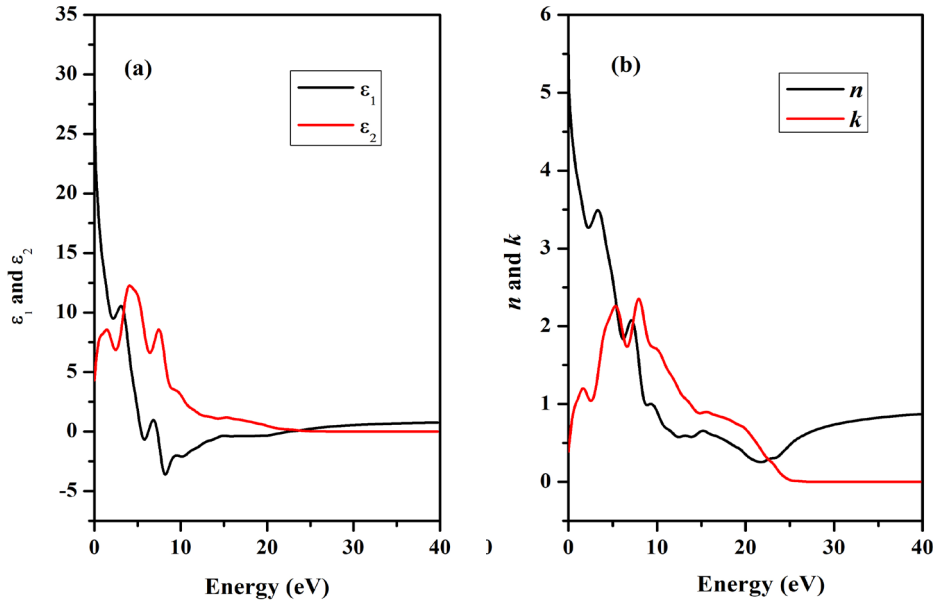

Figure 3: The real part $\varepsilon_1(\omega)$ and imaginary part $\varepsilon_2(\omega)$ of the dielectric function (**a**) and The refractive index $n(\omega)$ and the extinction coefficient $k(\omega)$ (**b**) of α-Cu_2Se.

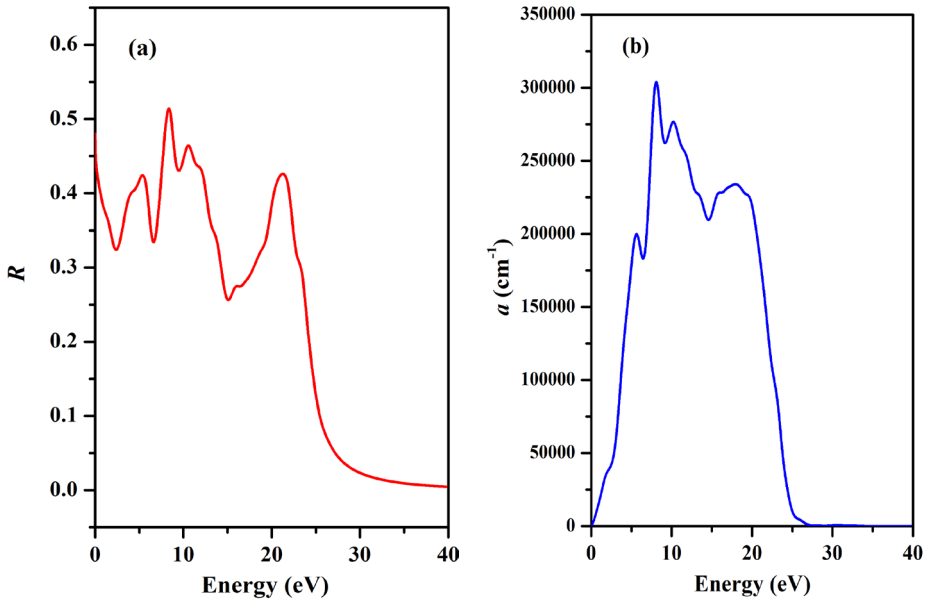

Figure 4: Reflectivity spectrum $R(\omega)$ (**a**) and absorption spectrum a (**b**) of α-Cu_2Se.

3.3 Elastic Properties

α-Cu_2Se adopts a cubic crystal structure, leading to the determination of its elastic constants as C_{11}, C_{12}, and C_{44}. The stability condition for a cubic crystal under pressure can be determined based on the Born stability criteria [15].

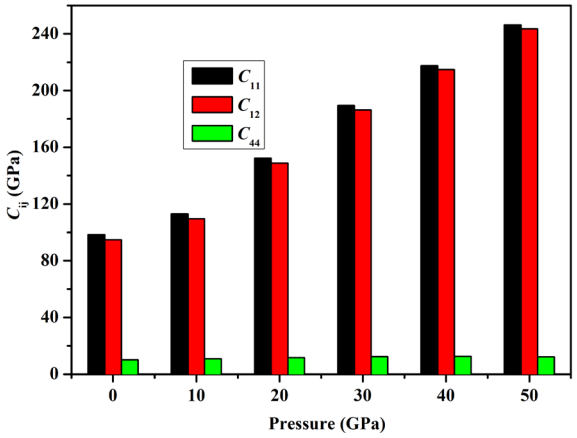

Figure 5: The Influence of pressure on the C_{ij} of α-Cu_2Se under varying pressure conditions.

As evidenced by the data presented in Table 2, α-Cu_2Se fulfills the mechanical stability criteria, demonstrating that the material remains mechanically stable under these conditions (0–50 GPa). The computed elastic constants of α-Cu_2Se align with the established stability conditions, further confirming the mechanical robustness of the crystal structure.

Table 2: Calculated C_{ij} (GPa) and B (GPa), G (GPa), E (GPa), υ, B/G of α-Cu_2Se under varying pressure conditions.

Pressure (GPa)	C_{11}	C_{12}	C_{44}	B	G	E	υ	B/G
0	98.4	94.7	10.2	95.9	5.25	15.5	0.473	18.3
10	113.1	109.5	10.9	110.7	5.43	16.0	0.476	20.4
20	152.4	148.8	11.7	150.0	5.69	16.8	0.481	26.3
30	189.5	186.3	12.5	187.4	5.75	17.1	0.484	32.6
40	217.5	214.7	12.6	215.6	5.56	16.5	0.487	38.8
50	246.2	243.6	12.3	244.5	5.35	15.9	0.489	45.7

Subsequently, within the elastic stability range of the α-Cu_2Se crystal (0–50 GPa), the Voigt-Reuss-Hill (VRH) method [16–18] was employed to estimate and analyze the B, G, E, and v under varying pressure conditions. In Table 3 and Fig. 6, the values of B, G, and E consistently rise as pressure increases. Since the B is significantly higher than the G at all pressure levels, it indicates that the α-Cu_2Se crystal demonstrates considerably lower resistance to shear deformation compared to compressive deformation. Young's modulus, which reflects a material's resistance to elastic deformation, also rises with pressure, suggesting an enhancement in the crystal's stiffness under higher pressure conditions. According to Pugh's criterion for mechanical behavior, a $B/G > 1.75$ suggests ductile behavior, whereas $B/G < 1.75$ indicates brittleness [19]. In this study, the calculated B/G values across all pressure levels are notably higher than 1.75, leading to the conclusion that α-Cu_2Se exhibits ductile characteristics.

Table 3: The values of β_{max} (TPa^{-1}), β_{min} (TPa^{-1}), G_{max} (GPa), G_{min} (GPa), E_{max} (GPa), E_{min} (GPa) of α-Cu_2Se at different pressures, respectively.

Pressure (GPa)	β_{max}	β_{min}	G_{max}	G_{min}	E_{max}	E_{min}
0	3.4746	3.4746	10.2	1.85	29.55	5.51
10	3.0111	3.0111	10.9	1.80	31.66	5.37
20	2.2222	2.2222	11.7	1.80	34.21	5.38
30	1.7790	1.7790	12.5	1.60	36.68	4.79
40	1.5458	1.5458	12.6	1.40	37.08	4.19
50	1.3635	1.3635	12.3	1.30	36.29	3.89

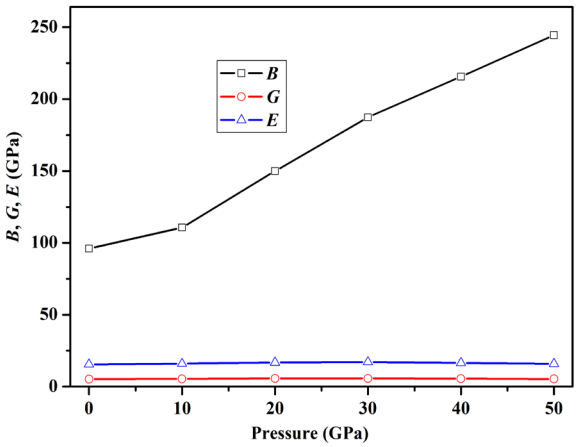

Figure 6: The Influence of pressure on the B, G, and E of α-Cu_2Se under varying pressure conditions.

Figs. 6–12 provide 2D views (projected onto the *xy*, *xz*, and *yz* planes) and 3D visualizations that illustrate the directional dependence of *E*, linear compressibility β, and *G* for α-Cu_2Se [20,21]. For both crystal structures, linear compressibility appears nearly isotropic across all planes. The graphical outputs, both in two and three dimensions, indicate that the level of anisotropy rises in the following order: $\beta < E < G$. Additionally, Table 3 summarizes the maximum and minimum values of *E*, β, and *G*. The elastic anisotropy under varying pressure conditions (0–50 GPa) is further quantified using the ratios β_{max}/β_{min}, G_{max}/G_{min}, and E_{max}/E_{min}. Higher values of these ratios correspond to greater anisotropy in the respective properties. The β_{max}/β_{min} ratios remain constant at 1 across all pressure levels (0 GPa to 50 GPa), indicating consistent isotropy in linear compressibility. In contrast, the G_{max}/G_{min} ratios are 1.3188, 1.3160, 1.2656, 1.2565, 1.2411, and 1.2309 at pressures of 0 GPa, 10 GPa, 20 GPa, 30 GPa, 40 GPa, and 50 GPa, respectively. Similarly, the E_{max}/E_{min} ratios are 1.2858, 1.2871, 1.2516, 1.2312, 1.1997, and 1.1815 at the same pressure points. From this data, it is evident that the anisotropic behavior of *G* and *E* diminishes as pressure increases, while β remains largely isotropic regardless of pressure changes.

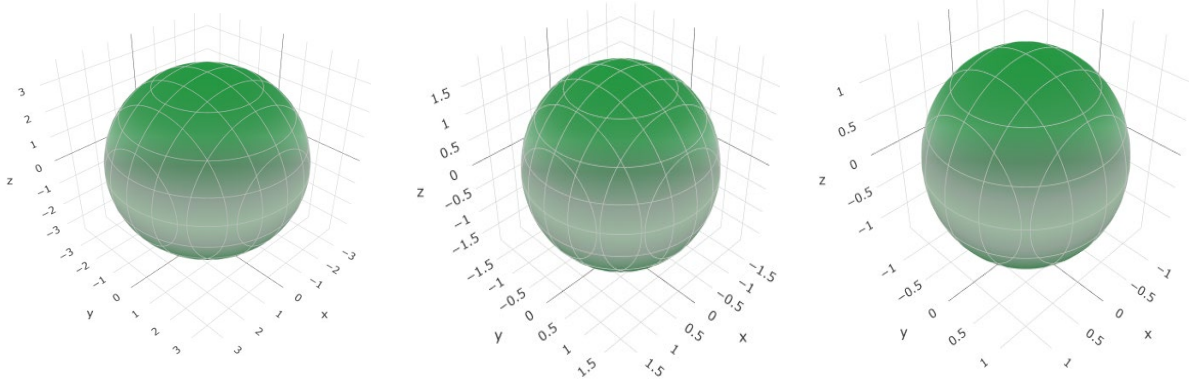

(0 GPa) (30 GPa) (50 GPa)

Figure 7: The β (TPa^{-1}) surface contours representation of α-Cu_2Se.

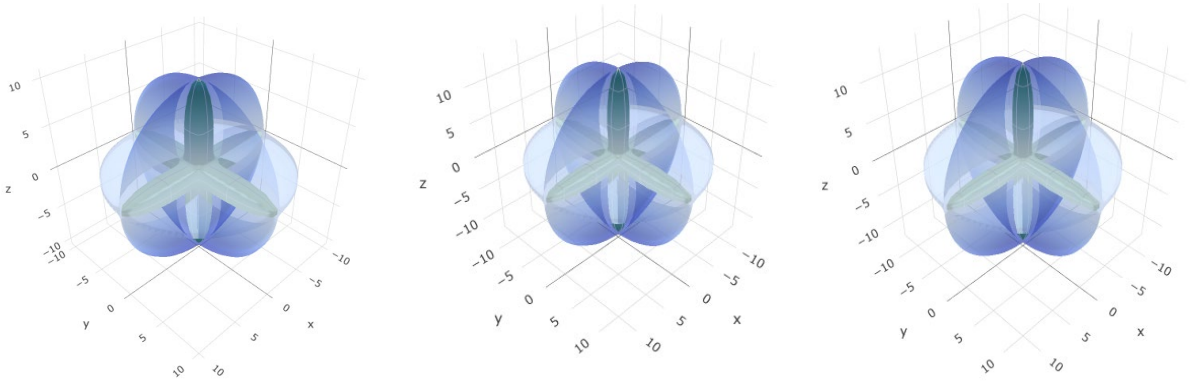

(0 GPa) (30 GPa) (50 GPa)

Figure 8: The G(GPa) surface contour representation of α-Cu_2Se.

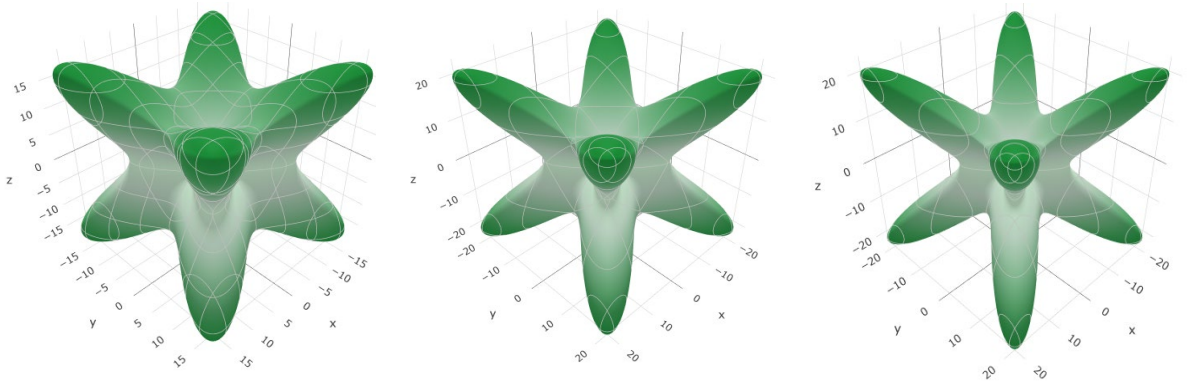

(0 GPa) (30 GPa) (50 GPa)

Figure 9: The E (GPa) surface contours representation of α-Cu_2Se.

(0 GPa)

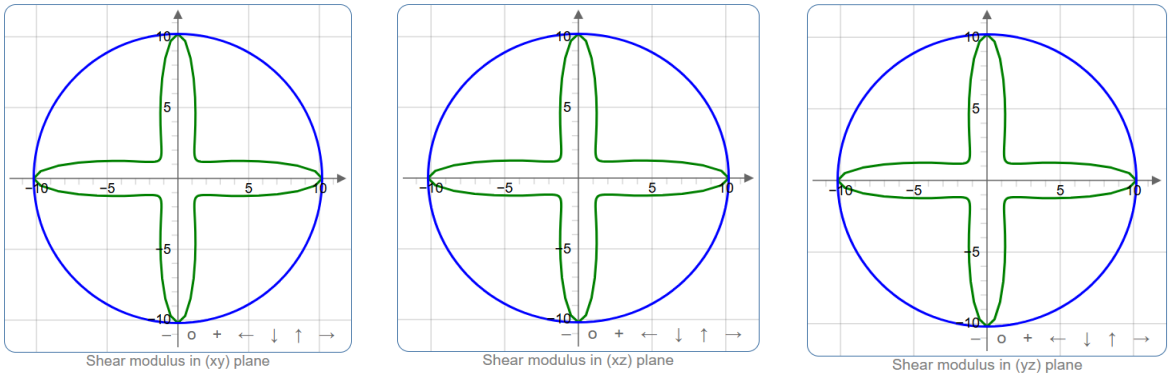

(30 GPa)

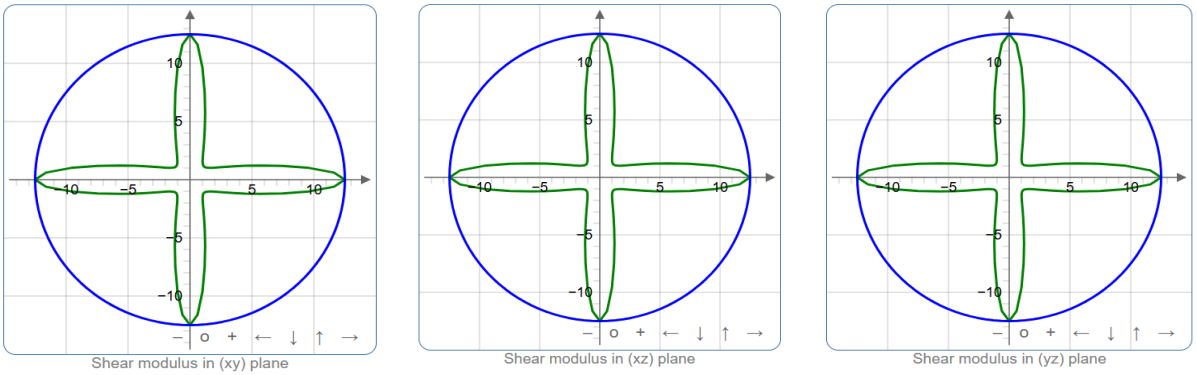

(50 GPa)

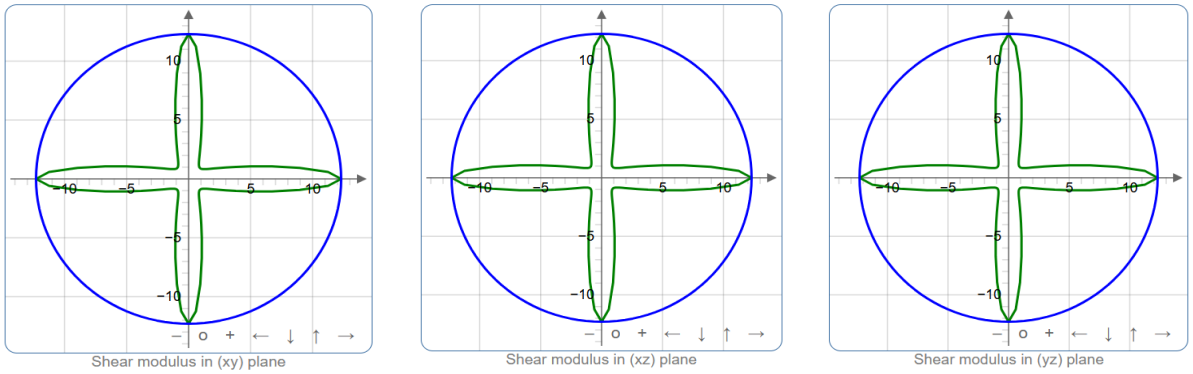

Figure 10: The representation of G(GPa) on different surfaces of α-Cu_2Se.

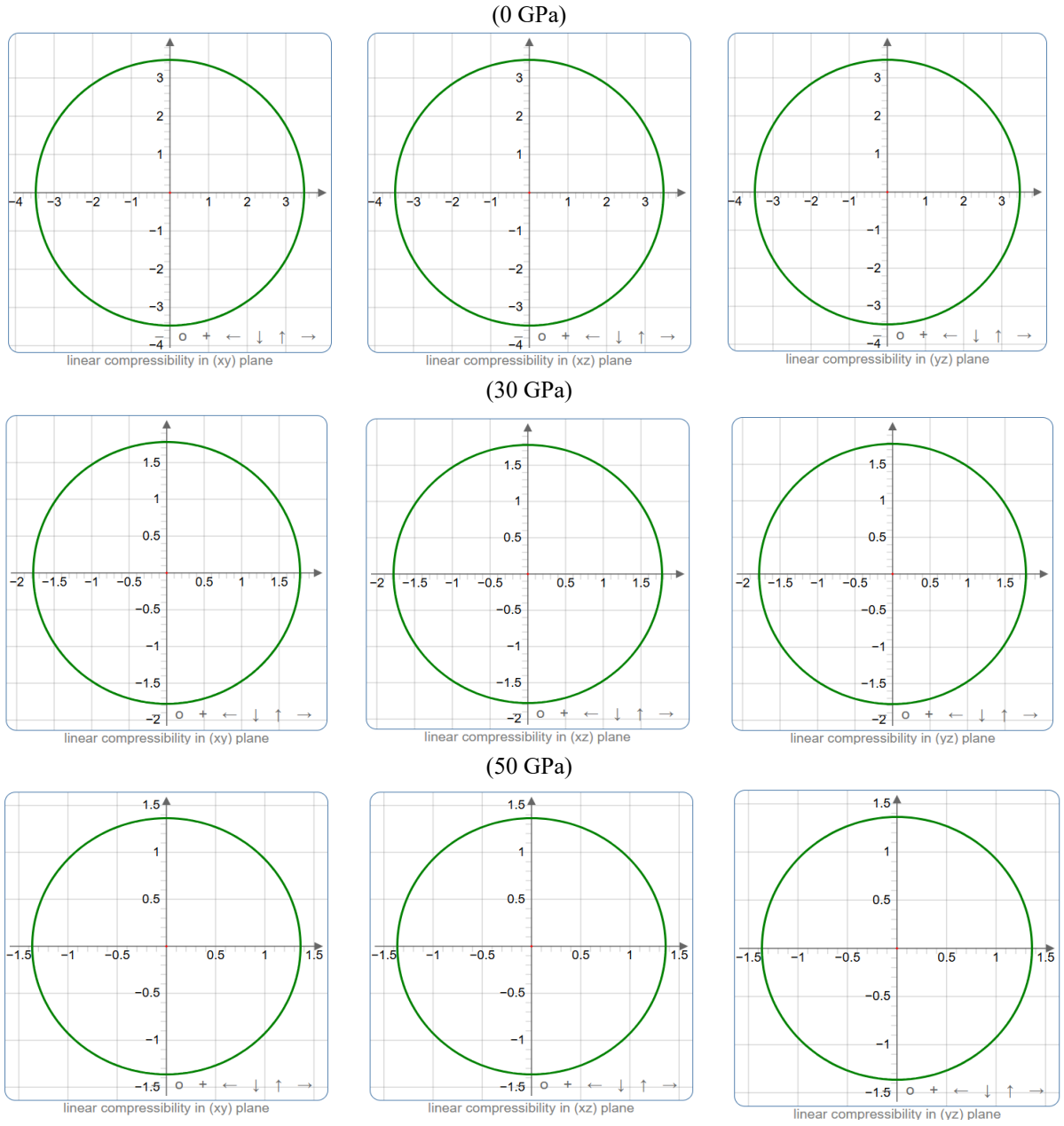

Figure 11: The representation of β (TP^{-1}) on different surfaces of α-Cu_2Se.

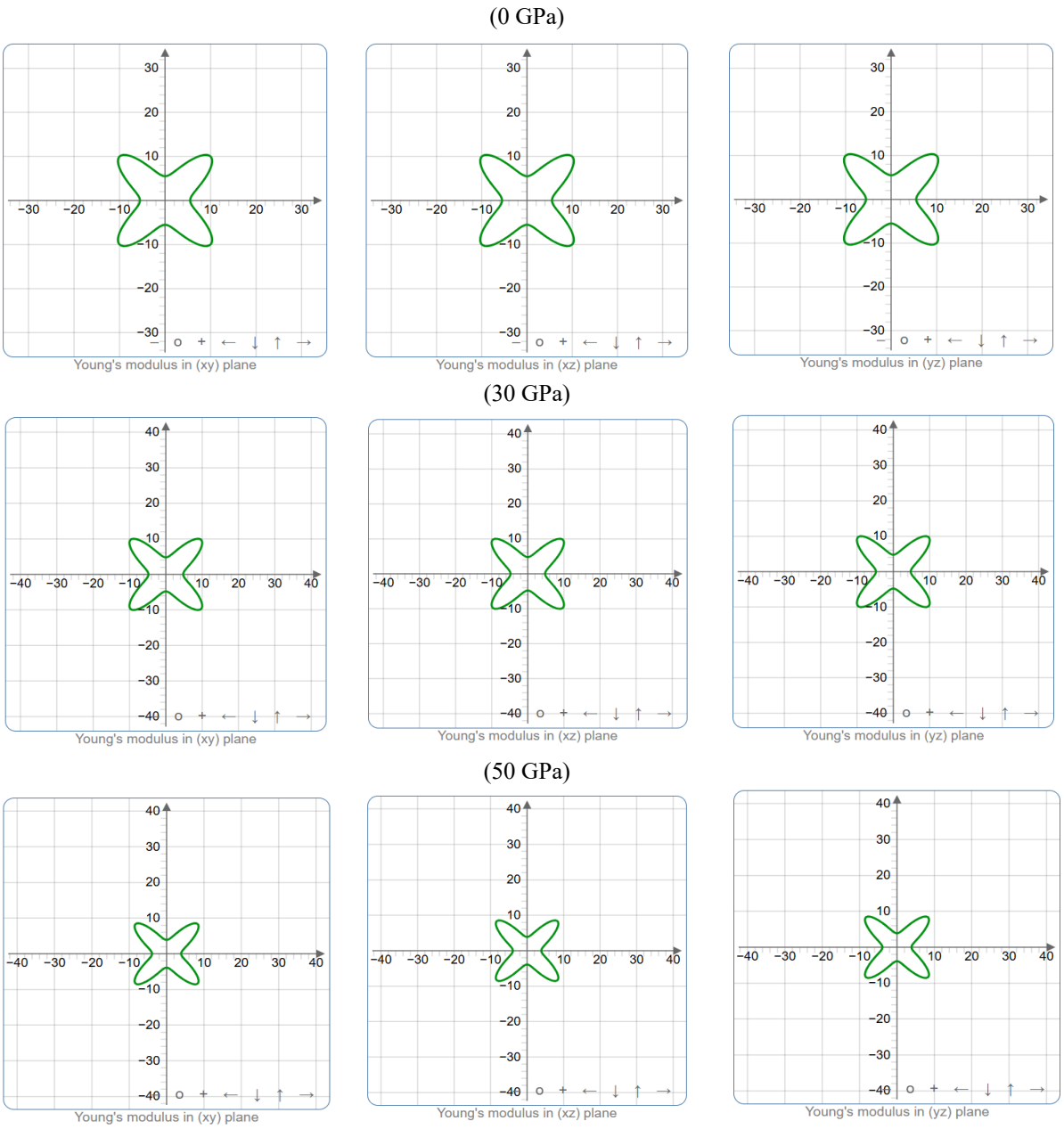

Figure 12: The representation of E (GPa) on different surfaces of α-Cu_2Se.

4 Conclusions

In conclusion, the physical characteristics of α-Cu_2Se have been systematically investigated using DFT. The calculated lattice parameters of the crystal structure show remarkable consistency with experimental measurements. The band structure and optical prpperties were also determined to provide insights into the α-Cu_2Se's properties. Furthermore, various elastic moduli were calculated to evaluate the elastic response of α-Cu_2Se under varying pressure conditions.

Acknowledgement: Not applicable.

Funding Statement: The authors received no specific funding for this study.

Author Contributions: The authors confirm contribution to the paper as follows: study conception and design: S. H. Fan, Y. S. Song; data collection: S. H. Fan; analysis and interpretation of results: S. H. Fan; draft manuscript preparation: S. H. Fan, Y. S. Song, H. J. Hou, H. L. Guo and S. R. Zhang. All authors reviewed the results and approved the final version of the manuscript.

Availability of Data and Materials: Not applicable.

Ethics Approval: Not applicable.

Conflicts of Interest: The authors declare no conflicts of interest to report regarding the present study

References

1. Okimura H, Matsumae T, Makabe R. Electrical properties of Cu_2−xSe thin films and their application for solar cells. Thin Solid Films. 1980;71:53–59. https://doi.org/10.1016/0040-6090(80)90183-2.
2. Chen WS, Stewart JM, Mickelsen RA. Polycrystalline thin-film Cu_2−xSe/CdS solar cell. Appl Phys Lett. 1985;46:1095–1097. https://doi.org/10.1063/1.95773.
3. Liu H, Shi X, Xu F, Zhang L, Zhang W, Chen L, Li Q, Uher C, Day T, Snyder GJ. Copper ion liquid-like thermoelectrics. Nat Mater. 2012;11:422–425. https://doi.org/10.1038/nmat3273.
4. Danilkin S, Skomorokhov A, Hoser A, Fuess H, Rajevac V, Bickulova N. Crystal structure and lattice dynamics of superionic copper selenide Cu_2−δSe. J Alloys Compd. 2003; 361:57–61. https://doi.org/10.1016/s0925-8388(03)00439-0.
5. Skomorokhov A, Trots D, Knapp M, Bickulova N, Fuess H. Structural behaviour of β-Cu_2−δSe (δ = 0, 0.15, 0.25) in dependence on temperature studied by synchrotron powder diffraction. J Alloys Compd. 2006;421:64–71. https://doi.org/10.1016/j.jallcom.2005.10.079.
6. Råsander M, Bergqvist L, Delin A. Density functional theory study of the electronic structure of fluorite Cu_2Se. J Physics Condens Matter. 2013;25:125503. https://doi.org/10.1088/0953-8984/25/12/125503.
7. Zhang Y, Shao X, Zheng Y, Yan L, Zhu P, Li Y, Xu H. Pressure-induced structural transitions and electronic topological transition of Cu_2Se. J Alloys Compd. 2018; 732:280–285. https://doi.org/10.1016/j.jallcom.2017.10.201.
8. Kresse G, Furthmüller J. Efficient iterative schemes forab initiototal-energy calculations using a plane-wave basis set. Phys Rev B. 1996;54:11169–11186. https://doi.org/10.1103/physrevb.54.11169.
9. Kresse G, Joubert D. From ultrasoft pseudopotentials to the projector augmented-wave method. Phys Rev B. 1999;59:1758–1775. https://doi.org/10.1103/physrevb.59.1758.
10. Perdew JP, Burke K, Ernzerhof M. Generalized gradient approximation made simple. Phys Rev Lett. 1996;77:3865–3868. https://doi.org/10.1103/PhysRevLett.77.3865.
11. Fan SH, Hou HJ, Guo HL. DFT study of elastic and thermodynamic properties of solar material Cu_2ZnSnS_4. J Ovonic Res. 2024;20:601–615. https://doi.org/10.15251/jor.2024.205.601.
12. Clark SJ, Segall MD, Pickard CJ, Hasnip PJ, Probert MIJ, Refson K, Payne MC. First Principles Methods Using CASTEP. Z Kristallogr/Cryst Mater. 2005;220:567–570, doi:10.1524/zkri.220.5.567.65075.
13. Vanderbilt D. Soft self-consistent pseudopotentials in a generalized eigenvalue formalism. Phys Rev B. 1990;41:7892–7895. https://doi.org/10.1103/physrevb.41.7892.
14. Heyding RD. The copper/selenium system. Can J Chem. 1966;44:1233–1236. https://doi.org/10.1139/v66-183.
15. Boudjemline A, Louail L, Islam MM, Diawara B. Dependence of pressure on elastic, electronic and optical properties of CeO_2 and ThO_2: A first principles study. Comput Mater Sci. 2011;50:2280–2286. https://doi.org/10.1016/j.commatsci.2011.03.006.
16. Voigt W. Lehrbuchder kristallphysik. Leipzig, Germany: Teubner Verlag; 1928.
17. Reuss A. Berechnung der Fließgrenze von Mischkristallen auf Grund der Plastizitätsbedingung für Einkristalle. ZAMM. 1929;9:49–58. https://doi.org/10.1002/zamm.19290090104.
18. Hill R. The Elastic Behaviour of a Crystalline Aggregate. Proc Phys Soc Sect A. 1952;65:349, doi:10.1088/0370-1298/65/5/307.
19. Pugh SFXCII. Relations between the elastic moduli and the plastic properties of polycrystalline pure metals. Lond Edinb Dublin Philos Mag J Sci. 1954;45:823–843. https://doi.org/10.1080/14786440808520496.
20. Gaillac R, Pullumbi P, Coudert F-X. ELATE: an open-source online application for analysis and visualization of elastic tensors. J Physics Condens Matter. 2016;28:275201–275201. http://doi.org/10.1088/0953-8984/28/27/275201.
21. Hou H-J, Chen W-X, Xiao L-X, Wang H-Y, Zhu H-J, Lu X-W, Zhang S-R, Guo H-L, Zhang Q-F. Effects of pressure on structural, mechanical, dynamics and thermal properties of Rankinite: Insights from first-principles calculations. Vacuum. 2023;213:112136. https://doi.org/10.1016/j.vacuum.2023.112136.